



Article

# CuInS<sub>2</sub>/Mg(OH)<sub>2</sub> Nanosheets for the Enhanced Visible-Light Photocatalytic Degradation of Tetracycline

Xiaogang Zheng <sup>1</sup>, Yiting Mao <sup>1</sup>, Jing Wen <sup>2,\*</sup>, Xiaojin Fu <sup>1</sup> and Xinhui Liu <sup>3,\*</sup>

<sup>1</sup> College of Chemistry and Chemical Engineering, Neijiang Normal University, Neijiang 641100, China; zhengxg123456@163.com (X.Z.); mao13566077755@163.com (Y.M.); fuxian2005@yahoo.com.cn (X.F.)

<sup>2</sup> Key Laboratory of Comprehensive and Highly Efficient Utilization of Salt Lake Resources, Key Laboratory of Salt Lake Resources Chemistry of Qinghai Province, Qinghai Institute of Salt Lakes, Chinese Academy of Sciences, Xining 810008, Qinghai, China

<sup>3</sup> State Key Laboratory of Water Environment Simulation, School of Environment, Beijing Normal University, Beijing 100875, China

\* Correspondence: wj580420@163.com (J.W.); xhliu@bnu.edu.cn (X.L.); Tel.: +86-0971-7762180 (J.W.); +86-0769-22862965 (X.L.)

Received: 9 October 2019; Accepted: 1 November 2019; Published: 5 November 2019



**Abstract:** CuInS<sub>2</sub>/Mg(OH)<sub>2</sub> (CIS/Mg(OH)<sub>2</sub>) nanosheets have been prepared for the visible light activated photodegradation of tetracycline hydrochloride (TCH). The introduction of CuInS<sub>2</sub> has proven to enhance the photocatalytic activity of Mg(OH)<sub>2</sub> nanosheets. It's ascribed to the enhanced transfer and separation of charge carriers at the junction interface between CuInS<sub>2</sub> and Mg(OH)<sub>2</sub>. The photocatalytic activity of obtained CIS/Mg(OH)<sub>2</sub> is greatly affected by CuInS<sub>2</sub> content, pH value, and inorganic ions. Among these samples, 2-CIS/Mg(OH)<sub>2</sub> exhibits the excellent photocatalytic activity and durability for the visible light driven removal of TCH after five cycle times. Atomic force microscope (AFM) images indicate that the surface roughness of 2-CIS/Mg(OH)<sub>2</sub> is intensively influenced in adsorption-photocatalysis process. The •O<sub>2</sub><sup>-</sup> and •OH radicals are vital for the visible light driven photocatalytic activity of 2-CIS/Mg(OH)<sub>2</sub> for TCH removal.

**Keywords:** CuInS<sub>2</sub>/Mg(OH)<sub>2</sub> nanosheets; heterojunction; tetracycline hydrochloride; photocatalysis

## 1. Introduction

Tetracycline hydrochloride (TCH, C<sub>22</sub>H<sub>24</sub>N<sub>2</sub>O<sub>8</sub>·HCl), as a broad-spectrum antibiotic, has been intensively applied for the therapy of human and livestock infections [1]. Due to the serious abuse and ineffective metabolization of TCH by the human body and livestock, its residue has become one of the largest source producers of non-biodegradable pollution damaging the human health and ecosystems [2,3]. Many strategies such as adsorption [4–6], biodegradation [7,8], coagulation [9], flotation [10], and advanced oxidation [11–14] are thus developed for the removal of TCH to reach a permissible level of ecological environment. As a typical advanced oxidation route, semiconductor-based photocatalysis has been paid great attention due to its low cost, non-pollution, and high efficiency [15–20]. In such a sustainable and green process, a proper semiconductor serves as the photocatalyst to participate in the oxidation reaction of TCH removal under solar light irradiation.

As a direct I-III-VI band gap semiconductor consisting of one divalent, one trivalent, and two divalent cations, copper indium sulfide (CuInS<sub>2</sub>) is considered as a potential visible-light photocatalyst owing to its narrow band gap (~1.5 eV), large optical absorption coefficient ( $\alpha > 10^5 \text{ cm}^{-1}$ ) and efficient solar energy conversion [21–23]. The phase structures such as wurtzite, zinc blende and chalcopyrite of CuInS<sub>2</sub> can greatly affect its luminescence property. For example, hexagonal CuInS<sub>2</sub> with wurtzite

structure is designed to enhance light-absorbing and to increase charge transfer because of the anisotropic crystal structure [24]. In addition, the abundant surface defects serve as the non-radiative recombination sites of charge carriers, accelerating the photocatalytic reaction on the surface of CuInS<sub>2</sub> [25]. Unfortunately, CuInS<sub>2</sub> suffers from the poor durability because of the photo-corrosion and surface oxidation under the long-term irradiation [26]. In fact, the acute photo-corrosion is ascribed to the excess holes assembled in the valence band of CuInS<sub>2</sub>. Therefore, the key issue of the enhanced stability and recyclability is to transfer the photoexcited holes from the valence band of CuInS<sub>2</sub>. Except for the hole-capture carrier and the sacrificial agents for the suppression of photoinduced corrosion, the heterojunction combined with at least two materials as well as has been confirmed to accelerate the hole transfer and enhance the stability [27–29]. For example, CuInS<sub>2</sub>/ZnS-TiO<sub>2</sub> [30], CuInS<sub>2</sub>/g-C<sub>3</sub>N<sub>4</sub> [31], CuInS<sub>2</sub>/Bi<sub>2</sub>WO<sub>6</sub> [32], rGO/CuInS<sub>2</sub> [33], and CuInS<sub>2</sub>/ZnS [34] have proven to expose the sufficient active sites and promote the transfer and separation of charge carriers at the junction interface. The efficient hole-capture materials are still explored for improving the hole transfer and affording the stability of CuInS<sub>2</sub>.

Magnesium hydroxide (Mg(OH)<sub>2</sub>), as a typical two-dimensional material with a type-II band structure, has been widely applied in photovoltaic devices and solid-state electronics owing to its rapid electron transport, low exciton recombination rate and efficient photon-harvesting capacity [35–44]. In contrast with the unstable or metastable two-dimensional materials such as black phosphorus, GaTe and MoTe<sub>2</sub>, the passivated surfaces created by O–H bonds composing of oxygen and hydrogen atoms are beneficial for the prolonged environmental stability of Mg(OH)<sub>2</sub> [36]. To further extend the application of Mg(OH)<sub>2</sub> in photocatalytic field, Mg(OH)<sub>2</sub>-based heterojunctions such as Mg(OH)<sub>2</sub>/WS<sub>2</sub> [40,41], Mg(OH)<sub>2</sub>/MoS<sub>2</sub> [42], and Mg(OH)<sub>2</sub>/AlN [43] have been designed for the extraordinary optical and electronic properties. Mg(OH)<sub>2</sub> based heterostructure can constantly separate the photoexcited electron-hole pairs and owns the decent band edge positions for photocatalytic redox reaction in the built-in electric field [45–47]. It's appealing and desirable to acquire Mg(OH)<sub>2</sub>-based heterojunctions for the visible light driven environmental remediation. To our best knowledge, there are no previous works about the enhanced photocatalytic activity of Mg(OH)<sub>2</sub> nanosheets coupled with CuInS<sub>2</sub>.

In this work, CuInS<sub>2</sub>-decorated Mg(OH)<sub>2</sub> (CIS/Mg(OH)<sub>2</sub>) nanosheets were developed for the visible light activated photocatalytic degradation of TCH. This heterojunction can modulate the interactions between Mg(OH)<sub>2</sub> nanosheets and CuInS<sub>2</sub> nanoparticles for the enhanced photocatalytic activity in visible region. CIS/Mg(OH)<sub>2</sub> heterojunction is expected to present better photocatalytic capacity than Mg(OH)<sub>2</sub> alone for the TCH removal.

## 2. Materials and Methods

### 2.1. Preparation of Catalysts

Mg(OH)<sub>2</sub> nanosheets were prepared via a hydrothermal approach. Briefly, 3 mmol magnesium nitrate (Mg(NO<sub>3</sub>)<sub>2</sub>·6H<sub>2</sub>O) and 1.0 g polyvinyl pyrrolidone (PVP, M = 58,000) were dispersed into 50 mL deionized water and then intensively stirred at room temperature for 2.0 h. Subsequently, ammonia solution (NH<sub>4</sub>OH, 25 wt. %) with a stoichiometric ratio of Mg<sup>2+</sup>/OH<sup>-</sup> (1:2) was slowly added into the above solution with an intensive stirring at room temperature for 3.0 h. The mixture solution was further transferred into a 100 mL Teflon-lined autoclave with the continuous heating at 423 K for 5.0 h. After cooling down to room temperature, the suspension was centrifuged, washed with deionized water for three times, and dried at 353 K for 5.0 h to obtain Mg(OH)<sub>2</sub> nanosheets.

CuInS<sub>2</sub>/Mg(OH)<sub>2</sub> composites were also prepared by a hydrothermal route. Typically, 0.1 g obtained Mg(OH)<sub>2</sub> bulks was dispersed into a 40 mL deionized water, and then cuprous chloride (CuCl), indium trichloride (InCl<sub>3</sub>·4H<sub>2</sub>O) and thioacetamide (CH<sub>3</sub>CSNH<sub>2</sub>) with their stoichiometric proportion were added into the above solution to achieve different loading content of CuInS<sub>2</sub> (3, 5, 7, and 9 wt. %). After stirred at room temperature for 2.0 h, this suspension was placed at a 50 mL Teflon-lined autoclave and heated at 433 K for 12.0 h. When cooled down to room temperature, the

above suspension was centrifuged, washed, and dried at 333 K for 10.0 h to obtain  $\text{CuInS}_2/\text{Mg}(\text{OH})_2$  with the  $\text{CuInS}_2$  content of 3, 5, 7 and 9 wt. %, which were respectively named as 1-CIS/ $\text{Mg}(\text{OH})_2$ , 2-CIS/ $\text{Mg}(\text{OH})_2$ , 3-CIS/ $\text{Mg}(\text{OH})_2$ , and 4-CIS/ $\text{Mg}(\text{OH})_2$ .

## 2.2. Characterization of Catalysts

CIS/ $\text{Mg}(\text{OH})_2$  composites were analyzed examined by X-ray diffraction (XRD, Bruker D8), field emission scanning electron microscopy (FE-SEM, Hitachi S-3400), transmission electron microscopy (TEM, FEI Tecnai G2 F20), X-ray photoelectron spectroscopy (XPS, Escalab 250), atomic force microscope (AFM, NT-MDT model BL222RNTE),  $\text{N}_2$  adsorption-desorption curves (NOVA-2020), inductively coupled plasma optical emission spectrometer (ICP-OES, Varian 710-ES), UV-Vis diffuse reflectance spectra (UV-Vis DRS, Hitachi U-4100) and Photoluminescence (PL, FLSP 920). The photoelectrochemical behaviors of these samples were investigated by a photoelectric instrument (CEL-PECX2000, Beijing CEL Tech. Co., Ltd., China) equipped with a Vertex. C. EIS (electrochemical impedance spectroscopy) electrochemistry workstation (Ivium Technologies B.V., Holland) and a Xe lamp of  $240 \text{ mW cm}^{-2}$ . In addition, the electron spin resonance (ESR, JES-FA200) was performed for the photoexcited radicals of obtained composites. The radicals trapped with 5,5-dimethyl-1-pyrroline-N-oxide (DMPO) were carried out in water for hydroxyl radical ( $\bullet\text{O}_2^-$ ) and methanol for superoxide radical ( $\bullet\text{O}_2^-$ ) in visible light region.

## 2.3. Photocatalytic Activity

CIS/ $\text{Mg}(\text{OH})_2$  composites were performed for the visible light activated photocatalytic degradation of TCH using a Xe lamp of 300 W ( $600 \text{ mW cm}^{-2}$ ) equipped with a cut-off wavelength of 420 nm as the light source. In a typical process, 50 mg obtained bulks were dispersed into a 100 mL TCH solution and then stirred at room temperature in dark for 2.0 h to reach the adsorption-desorption equilibrium. After irradiated at an interval time, 5 mL TCH solution was sampled, filtered, and analyzed using an Agilent 1100 with a  $5 \mu\text{m}$ ,  $4.6 \times 250 \text{ mm}$  Venusil HILIC column and an ultraviolet detector of 356 nm. The Effects of  $\text{CuInS}_2$  content, inorganic ions, pH value and quenching agents on the photocatalytic activity of CIS/ $\text{Mg}(\text{OH})_2$  were also investigated according to the above process. The intermediate products of TCH were detected by an UPLC-MS system (Waters UPLC Acquity, Quattro Premier XE).

## 3. Results

Figure S1 shows the XRD patterns of  $\text{Mg}(\text{OH})_2$  and CIS/ $\text{Mg}(\text{OH})_2$ . The typical peaks at  $18.5^\circ$ ,  $32.7^\circ$ ,  $37.9^\circ$ ,  $51.2^\circ$ ,  $58.5^\circ$ ,  $62.0^\circ$ ,  $68.0^\circ$ , and  $72.0^\circ$  are assigned to the (001), (100), (101), (102), (110), (111), (103), and (201) facets of hexagonal  $\text{Mg}(\text{OH})_2$  (JCPDS, 07-0239), respectively [38,39]. The diffraction peaks belonging to  $\text{CuInS}_2$  were not observed in XRD patterns of CIS/ $\text{Mg}(\text{OH})_2$  due to its low content, low crystallinity and high dispersion [30]. In contrast with pure  $\text{Mg}(\text{OH})_2$ , the peak positions of  $\text{Mg}(\text{OH})_2$  phases are shifted to the higher values by the introduction of  $\text{CuInS}_2$ .

SEM images (Figure S2) reveal that pure  $\text{Mg}(\text{OH})_2$  is irregular flake-like structure with an average thickness of around 20 nm. The introduction of  $\text{CuInS}_2$  induce to the serious agglomeration degree of CIS/ $\text{Mg}(\text{OH})_2$  in comparison to pure  $\text{Mg}(\text{OH})_2$ , as shown in Figure 1. With the increasing  $\text{CuInS}_2$  content, the agglomeration degree of CIS/ $\text{Mg}(\text{OH})_2$  composites decreases, while their average thickness of nanosheets increases. In contrast with the sphere-like clusters of 1-CIS/ $\text{Mg}(\text{OH})_2$  with a nominal  $\text{CuInS}_2$  content of 3.0 wt. % (Figure 1A,B), 2-CIS/ $\text{Mg}(\text{OH})_2$  with a nominal  $\text{CuInS}_2$  content of 5.0 wt. % (Figure 1C,D) becomes weaker agglomeration, which are further confirmed by TEM images (Figure 2A,B). It's noticed that  $\text{CuInS}_2$  nanoparticles of around 1.0 nm (Figure 2C,D) are well distributed in  $\text{Mg}(\text{OH})_2$  nanosheets. The spacing distances of typical lattices of  $\text{Mg}(\text{OH})_2$  (101) and  $\text{CuInS}_2$  (112) planes are 0.24 nm and 0.32 nm, respectively [32,39]. Based on the TEM image of 2-CIS/ $\text{Mg}(\text{OH})_2$  (Figure S3), elemental mapping images (Figure 2E-I) also indicate that there are Mg, O, Cu, In, and S elements exist in 2-CIS/ $\text{Mg}(\text{OH})_2$ , meaning the successful synthesis of  $\text{CuInS}_2/\text{Mg}(\text{OH})_2$  composites. H element was not detected by elemental mapping. The  $\text{N}_2$  adsorption-desorption curves of obtained

CIS/Mg(OH)<sub>2</sub> (Figure S4) are the type IV isotherms, meaning the formation of mesopores and/or macropores structures. As listed in Table S1, the introduction of CuInS<sub>2</sub> on the surface and pore structure of Mg(OH)<sub>2</sub> induces to the decrease in specific surface area and pore volume.

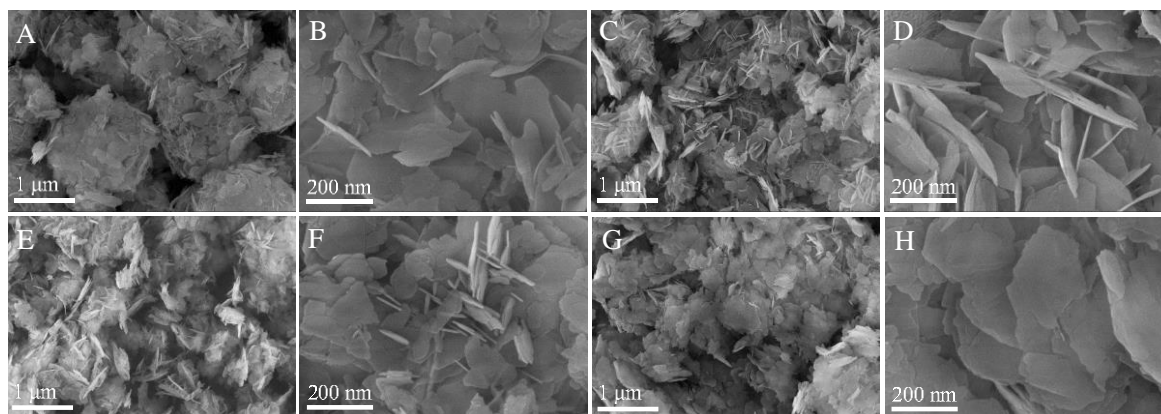


**Figure 1.** Scanning electron microscopy (SEM) images of 1-CIS/Mg(OH)<sub>2</sub> (A,B), 2-CIS/Mg(OH)<sub>2</sub> (C,D), 3-CIS/Mg(OH)<sub>2</sub> (E,F), and 4-CIS/Mg(OH)<sub>2</sub> (G,H).

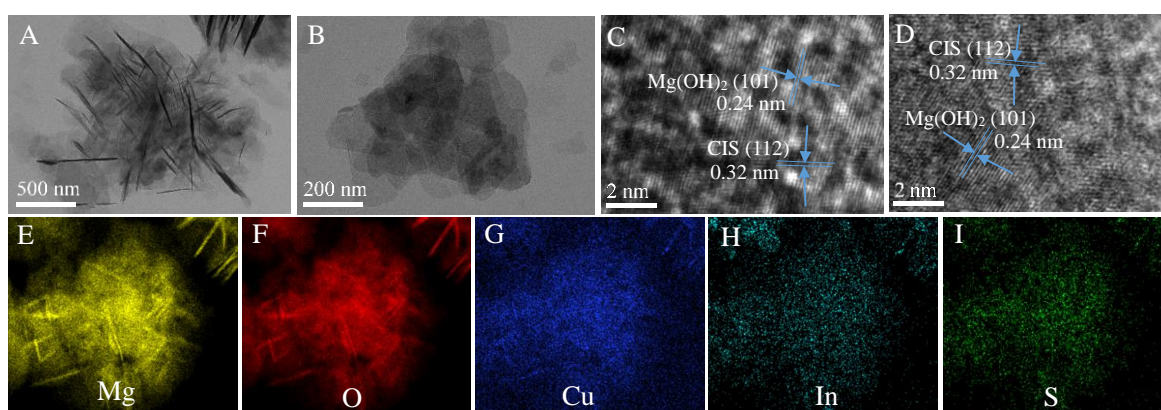


**Figure 2.** Transmission electron microscopy (TEM) images (A,B), high resolution transmission electron microscope (HRTEM) images (C,D), and elemental mapping images (E–I) of 2-CIS/Mg(OH)<sub>2</sub>.

As shown in Figure 3, the Mg, Cu, O, In, and S elements exist in the survey XPS spectra of fresh and used 2-CIS/Mg(OH)<sub>2</sub>, of which the used sample was collected after five cycle times for the visible-light driven photodegradation of TCH under the same conditions. The long-term irradiation induces to the difference in XPS spectra (Figure 3B–F) and metallic contents (Table S1) of fresh and used 2-CIS/Mg(OH)<sub>2</sub>. Compared with fresh sample (1303.4 eV), Mg 1s peak of used 2-CIS/Mg(OH)<sub>2</sub> (Figure 4B) shifts to a lower binding energy (1303.2 eV). O 1s peaks belonging to lattice oxygen (Figure 4C) of fresh and used 2-CIS/Mg(OH)<sub>2</sub> locate at 531.45 and 531.34 eV, respectively. As shown in Figure 3D, the two splitting peaks indexing to Cu 2p<sub>1/2</sub> and Cu 2p<sub>3/2</sub> respectively appear at 952.2 eV and 932.6 eV in fresh sample, while these peaks of used sample migrate to higher binding energies (952.5 and 932.8 eV). In contrast with fresh sample (452.6 and 445.2 eV), the peaks of In 3d<sub>3/2</sub> and In 3d<sub>5/2</sub> in used sample (Figure 3E) shift to the lower binding energies (452.5 and 445.1 eV). The splitting peaks of fresh 2-CIS/Mg(OH)<sub>2</sub> at 162.8 and 161.7 eV are respectively indexed to S 2p<sub>1/2</sub> and S 2p<sub>3/2</sub>, while these peaks of used sample respectively immigrate to 163.1 and 161.6 eV (Figure 3F).

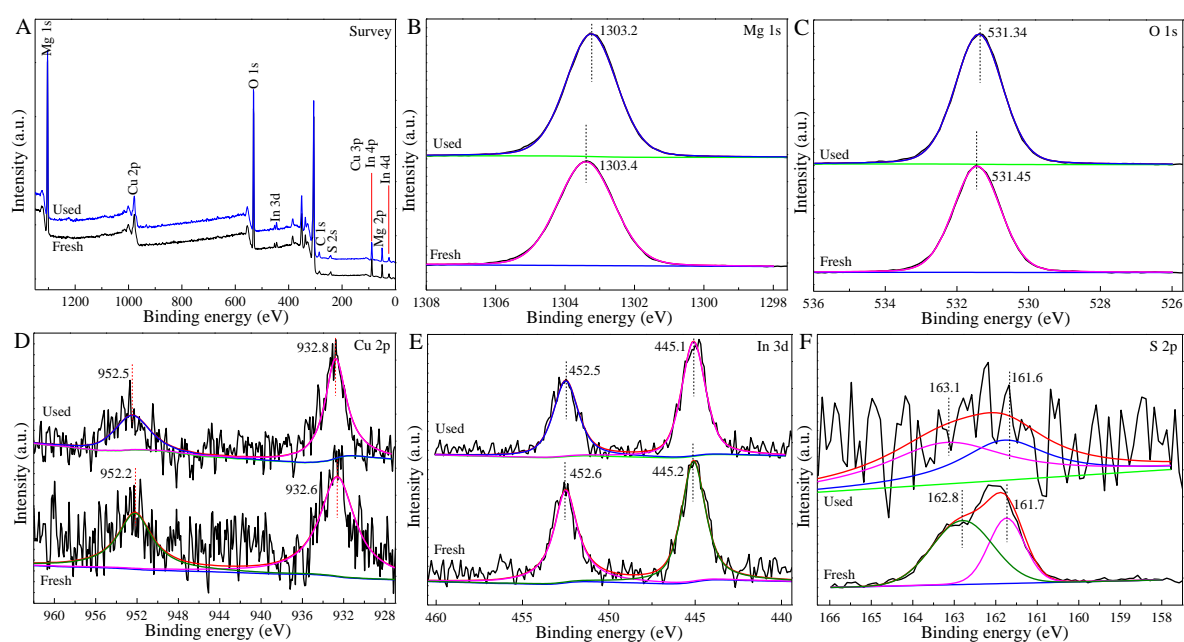


**Figure 3.** Survey (A), Mg 1s (B), O 1s (C), Cu 2p (D), In 3d (E), and S 2p (F) X-ray photoelectron spectroscopy (XPS) spectra of fresh and used 2-CIS/Mg(OH)<sub>2</sub>.

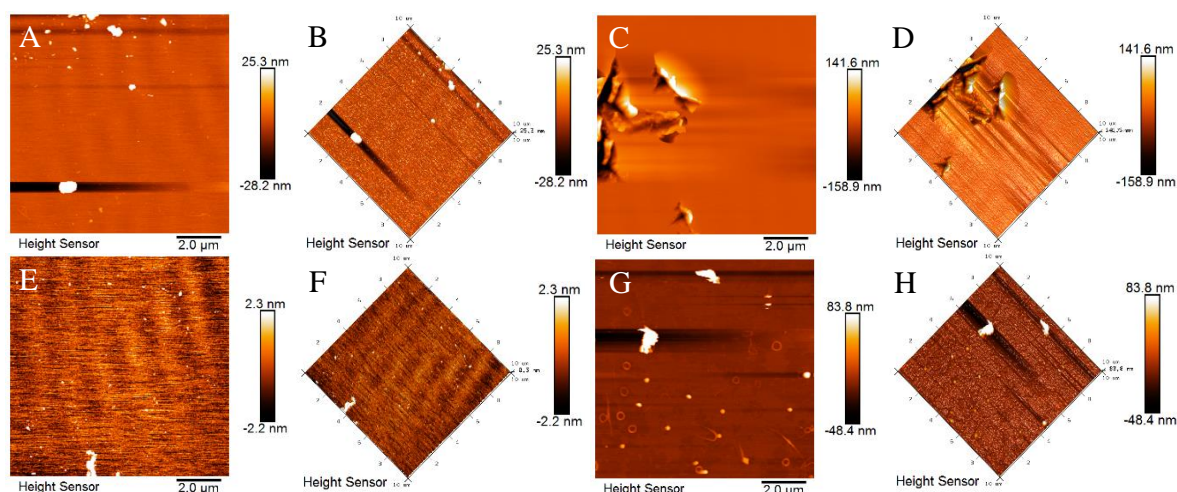


**Figure 4.** 2D and 3D atomic force microscope (AFM) images of fresh (A,B), adsorbed (C,D), photocatalytic (E,F), and used 2-CIS/Mg(OH)<sub>2</sub> (G,H).

Surface roughness of 2-CIS/Mg(OH)<sub>2</sub> in different stages of photocatalytic system was observed by AFM, including the fresh, adsorbed with TCH in dark after 2.0 h, visible-light driven photocatalytic reaction after 30 min (photocatalytic) and used ones after visible-light irradiation time of 60 min (Figure 4). These adsorbed, photocatalytic, and used samples were obtained from the adsorption–photocatalysis process and not further washed with deionized water. The parameters such as average roughness ( $R_a$ ), root mean square roughness ( $R_q$ ), and surface skewness ( $S_{sk}$ ) obtained by Nanoscope analysis software (Table S2) were employed to describe the surface roughness of 2-CIS/Mg(OH)<sub>2</sub> in the sorption-photocatalysis process for the TCH removal [48]. Due to the interface dependence of sorption-photocatalytic reaction, high surface roughness values are likely to facilitate the adsorption and photocatalysis processes, while the excessively high surface roughness induces to the mechanical and structural collapse [49]. Due to the efficient adsorption capacity and thin interpenetration layer of TCH molecules on the active sites, the  $R_a$  (44.2 nm),  $R_q$  (58.7 nm), and  $S_{sk}$

(0.45) values of this sample after adsorbed for 2.0 h at room temperature are higher than those values (8.9 nm, 15.40 nm, and 2.80) of fresh 2-CIS/Mg(OH)<sub>2</sub>. However, those parameters of surface roughness decrease with the increasing reaction time during the photocatalysis process, meaning the efficient conversion of TCH into small molecules and the rapid diffusion of small molecules from the bulks surface to aqueous solution. The  $R_a$ ,  $R_q$ , and  $S_{sk}$  values of 2-CIS/Mg(OH)<sub>2</sub> after irradiated 30 min are respectively 1.77 nm, 3.09 nm, and 3.06, which are higher those values (1.20 nm, 1.62 nm, and 1.00) of sample after irradiated 60 min. The reduced surface roughness of 2-CIS/Mg(OH)<sub>2</sub> under long-time visible light irradiation may be ascribed to the inferior diffusion of small molecules from the active sites and photo-corrosion.

These CIS/Mg(OH)<sub>2</sub> samples exhibit two absorption wavelengths of 200~250 nm and 250~800 nm, as shown in Figure 5A. The introduction of CuInS<sub>2</sub> into Mg(OH)<sub>2</sub> nanosheets can enhance the visible-light adsorption ability due to the combined effect between n-type Mg(OH)<sub>2</sub> and p-type CuInS<sub>2</sub> [39]. Among these composites, 2-CIS/Mg(OH)<sub>2</sub> presents the best visible-light harvesting capacity. The adequate coupling of p–n semiconductors is favorable for the charge transfer and the charge carrier's separation [50,51]. It's noticed that PL intensity of CIS/Mg(OH)<sub>2</sub> is to some extent weaker than that of Mg(OH)<sub>2</sub> nanosheets, especially 2-CIS/Mg(OH)<sub>2</sub> (Figure 5B). Visible light activated photocurrent responses (Figure 5C) indicates that the photocurrent intensity of 2-CIS/Mg(OH)<sub>2</sub> is higher than that of X-CIS/Mg(OH)<sub>2</sub> (X = 1, 3, and 4). In addition, small arc radius of electrochemical impedance spectroscopy is also obtained by 2-CIS/Mg(OH)<sub>2</sub> (Figure 5D). It's further indicated that the CuInS<sub>2</sub> can enhance the charge transfer and restrain the recombination of photoinduced electron-hole pairs of Mg(OH)<sub>2</sub> via the efficient junction interface, strengthening the photocatalytic activity.

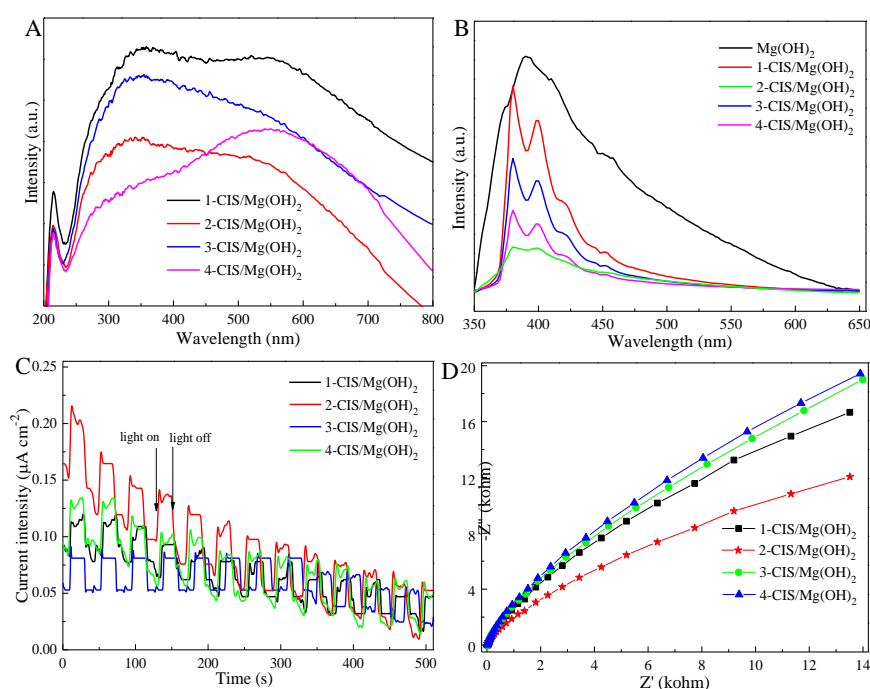


**Figure 5.** UV-Vis absorption spectra (A), Photoluminescence (PL) spectra (B), photocurrent-time response (C) and electrochemical impedance spectroscopy (EIS) Nyquist plots (D) of CIS/Mg(OH)<sub>2</sub>.

CIS/Mg(OH)<sub>2</sub> composites were performed for the photocatalytic degradation of TCH in the visible light region. The texture structure and naked active sites greatly affect the adsorption capacity and photocatalytic activity [33,51,52]. In contrasted with pure Mg(OH)<sub>2</sub> nanosheets, CuInS<sub>2</sub> nanoparticles loaded onto Mg(OH)<sub>2</sub> induces to the inferior adsorption capacity while it enhances the photocatalytic activity under the same conditions (Table S3). As shown in Figure 6A, the photocatalytic activity of CIS/Mg(OH)<sub>2</sub> increases and then decreases with an increase in CuInS<sub>2</sub> content, of which 2-CIS/Mg(OH)<sub>2</sub>

exhibits the best photocatalytic performance in TCH removal. It's attributed to the efficient generation and transfer of charge carriers at the junction interface between  $\text{CuInS}_2$  nanoparticles and  $\text{Mg}(\text{OH})_2$  nanosheets. However, excess of  $\text{CuInS}_2$  bulk loaded on the  $\text{Mg}(\text{OH})_2$  serves as the recombination center of photoinduced electron and holes, leading to the inferior photocatalytic activity [28,47]. As shown in Figure 6B, the photocatalytic activity of 2-CIS/ $\text{Mg}(\text{OH})_2$  increases and then decreases with the increasing pH value below 7.0, while decreases with an increase in pH value above 7.0. Hence, the optimal pH value is 4.65 for the photocatalytic performance of 2-CIS/ $\text{Mg}(\text{OH})_2$  (Table S4). The acidic condition is much more suitable for the visible-light driven photodegradation of TCH in comparison with the alkaline condition. This reason is that the amount of radicals such as  $\bullet\text{O}_2^-$  and  $\bullet\text{OH}$  are greatly related with pH value. The  $\text{OH}^-$  (or  $\text{H}^+$ ) ions can react with the photoexcited  $e^-/h^+$  pairs to form radical species such as  $\bullet\text{O}_2^-$  and  $\bullet\text{OH}$ , which are crucial for the photocatalytic reaction of TCH degradation [52,53]. The chain reactions for the photo-activated radicals are seriously quenched by excess of  $\text{OH}^-$  and  $\text{H}^+$  ions, leading to the inferior photocatalytic activity. In addition, inorganic ions play an important role in the visible light driven photocatalytic capacity. The addition of inorganic ions can not only affect the pH value of TCH solution, but also scavenge the radical species in the photocatalytic system [51,54]. It's noticed that the inorganic ions such as  $\text{NaCl}$ ,  $\text{Na}_2\text{SO}_4$ ,  $\text{Na}_2\text{CO}_3$ , and  $\text{Na}_3\text{PO}_4$  restrain the photocatalytic capacity of 2-CIS/ $\text{Mg}(\text{OH})_2$  for TCH removal in visible light region (Figure 6C and Table S5). 2-CIS/ $\text{Mg}(\text{OH})_2$  slightly deactivates for the visible light driven degradation of TCH after five cycle times (Figure 6D), indicating the excellent durability and recyclability of 2-CIS/ $\text{Mg}(\text{OH})_2$ . This was further confirmed by XRD, SEM images, and XPS. Compared with fresh 2-CIS/ $\text{Mg}(\text{OH})_2$ , the XRD pattern (Figure S5) and morphology structure (Figure S6) of used sample are not changed. However, the surface composition (Figure 3) is changed due to the long-time irradiation in visible light region.

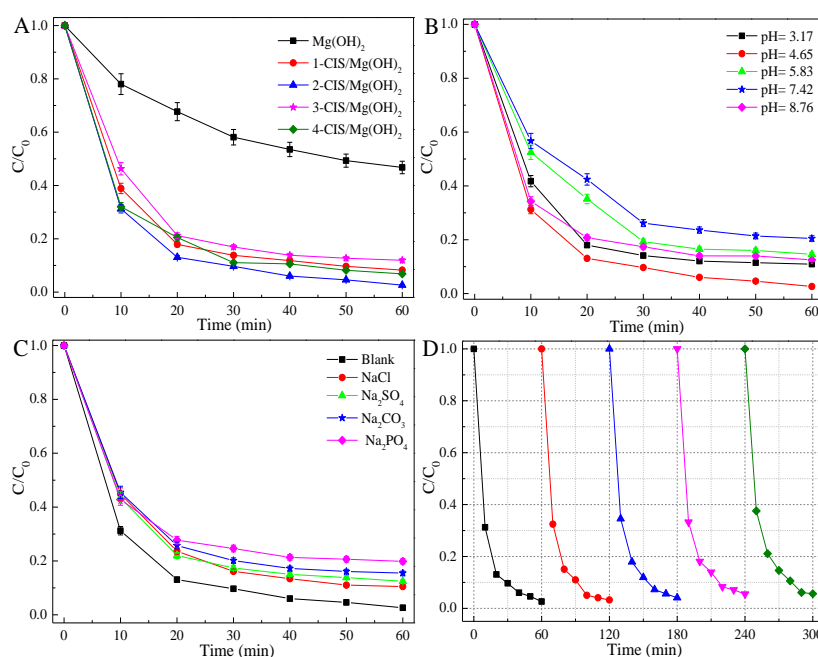


**Figure 6.** Effect of  $\text{CuInS}_2$  content (A), pH value (B) and inorganic ions (C) on the photocatalytic activity of CIS/ $\text{Mg}(\text{OH})_2$  composites and the photocatalytic stability (D) of 2-CIS/ $\text{Mg}(\text{OH})_2$ .

The radical species such as  $\bullet\text{O}_2^-$  and  $\bullet\text{OH}$  were evaluated by ESR. The ESR signals intensities of DMPO- $\bullet\text{O}_2^-$  in methanol (Figure 7A) are stronger than those of DMPO- $\bullet\text{OH}$  in aqueous (Figure 7B), which further strengthen with an increase in the irradiation time. It's suggested that  $\bullet\text{O}_2^-$  radical plays a crucial role in the photocatalytic reaction of 2-CIS/ $\text{Mg}(\text{OH})_2$ , which is further evaluated by the quenching test. The addition of scavengers (0.1 mmol) such as tert-butyl alcohol (*t*-BuOH),

*p*-benzoquinone (*p*-BQ) and ethylenediamine tetraacetic acid disodium salt (EDTA-2Na) into the photocatalytic system can restrain the photocatalytic activity of 2-CIS/Mg(OH)<sub>2</sub> (Figure 7C). Compared with EDTA-2Na and *t*-BuOH, the photocatalytic activity of 2-CIS/Mg(OH)<sub>2</sub> is greatly suppressed by the addition of *p*-BQ. It's suggested that •O<sub>2</sub><sup>-</sup> radical is the vital radical for the TCH removal.

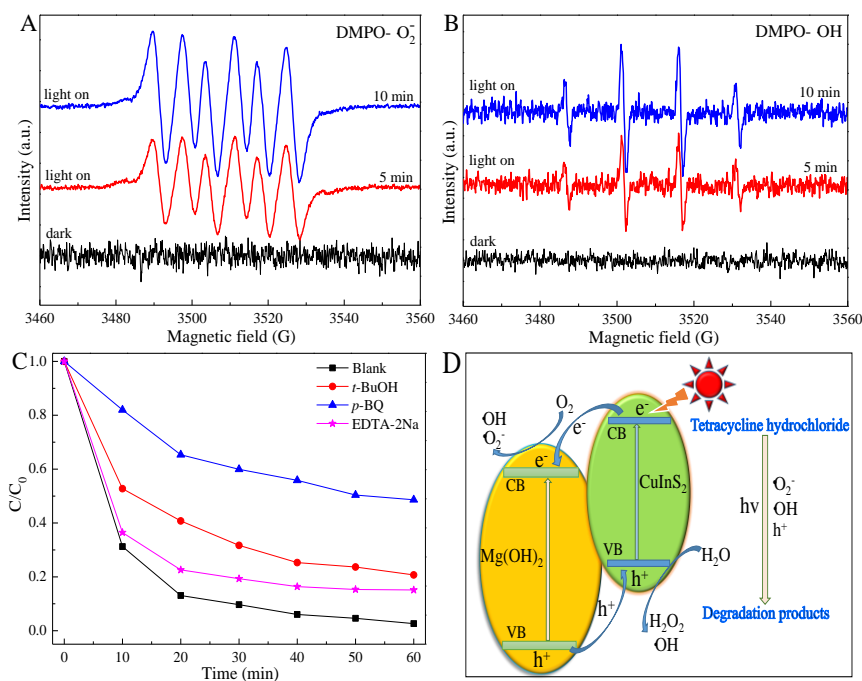


**Figure 7.** Electron spin resonance (ESR) spectra of DMPO-O<sub>2</sub><sup>-</sup> in methanol (A) and DMPO-OH in aqueous (B), quenching test (C), and photocatalytic mechanism (D) of 2-CIS/Mg(OH)<sub>2</sub>.

The possible photocatalytic mechanism of 2-CIS/Mg(OH)<sub>2</sub> is proposed in Figure 7D. In this heterojunction structure, the photoexcited electrons generated from the valence band (VB) of CuInS<sub>2</sub> are transferred from the conduction band (CB) of CuInS<sub>2</sub> to the CB of Mg(OH)<sub>2</sub>, meanwhile the h<sup>+</sup> radicals formed from VB of Mg(OH)<sub>2</sub> are migrated to VB of CuInS<sub>2</sub>. This facilitates the repaired transfer and separation of photoexcited e<sup>-</sup> and H<sup>+</sup>, leading to the efficient photocatalytic activity. Dissolved O<sub>2</sub> molecules can react with e<sup>-</sup> to form •O<sub>2</sub><sup>-</sup> and •OH radicals, and H<sub>2</sub>O molecules can react with h<sup>+</sup> to generate •OH radical. These radicals can efficiently attacked TCH molecules into small molecules through the demethylation, hydroxylation, deamination, N-C bond cleavage, loss of NH<sub>3</sub> and H<sub>2</sub>O (Figures S7 and S8), which can be further strengthened with the increasing irradiation time to generate non-toxic molecules [8,55]. The enhanced photocatalytic capacity of 2-CIS/Mg(OH)<sub>2</sub> composite is achieved for the visible light driven degradation of TCH compared with the previous works, as listed in Table S6. Especially, TiO<sub>2</sub> is not excited in visible light region but in UV-light region, and its photocatalytic activity is greatly affected by its microstructure, crystalline phases, and naked lattice planes [56–60]. 2-CIS/Mg(OH)<sub>2</sub> can be considered as an efficient photocatalyst for the visible-light driven treatment of wastewaters such textile and antibiotics effluents in industrial application.

#### 4. Conclusions

CIS/Mg(OH)<sub>2</sub> nanosheets exhibit the better photocatalytic activity in comparison to Mg(OH)<sub>2</sub> for the visible light driven degradation of TCH. The combined effect between CuInS<sub>2</sub> and Mg(OH)<sub>2</sub> is likely to enhance the photocatalytic activity. The surface roughness of 2-CIS/Mg(OH)<sub>2</sub> is changed in adsorption-photocatalytic system. ESR results indicate that •O<sub>2</sub><sup>-</sup> radical as well as •OH is the main radical for the enhanced photocatalytic activity of 2-CIS/Mg(OH)<sub>2</sub>. Among these obtained composites,



2-CIS/Mg(OH)<sub>2</sub> with the nominal CuInS<sub>2</sub> content 5.0 wt. % presents the best photocatalytic activity and stability after five cycle times under the same conditions.

**Supplementary Materials:** The following are available online at <http://www.mdpi.com/2079-4991/9/11/1567/s1>, Figure S1: XRD patterns of Mg(OH)<sub>2</sub> and CIS/Mg(OH)<sub>2</sub>, Figure S2: SEM images of Mg(OH)<sub>2</sub>, Figure S3: TEM images of 2-CIS/Mg(OH)<sub>2</sub>, Figure S4: N<sub>2</sub> adsorption-desorption curves of CIS/Mg(OH)<sub>2</sub> with varying CuInS<sub>2</sub> content, Figure S5: XRD patterns of fresh and used 2-CIS/Mg(OH)<sub>2</sub>, Figure S6: SEM images of used 2-CIS/Mg(OH)<sub>2</sub>, Figure S7: HPLC/MS spectrum of TCH solution under visible-light irradiation of 30 min over 2-CIS/Mg(OH)<sub>2</sub>, Figure S8: HPLC/MS spectrum of TCH solution under visible-light irradiation of 60 min over 2-CIS/Mg(OH)<sub>2</sub>; Table S1: Texture parameters of CIS/Mg(OH)<sub>2</sub>-based samples, Table S2: The parameters of Surface roughness of 2-CIS/Mg(OH)<sub>2</sub>, Table S3: The adsorption-photocatalysis capacities of CIS/Mg(OH)<sub>2</sub> samples, Table S4: Effect of pH value on the adsorption-photocatalysis capacities of 2-CIS/Mg(OH)<sub>2</sub>, Table S5: Effect of inorganic ions on the adsorption-photocatalysis capacities of 2-CIS/Mg(OH)<sub>2</sub>, Table S6: Comparison of photocatalytic performance for removal of organic pollutants.

**Author Contributions:** Conceptualization, formal analysis and writing—original draft preparation, X.Z.; validation, project administration and funding acquisition, X.L.; investigation and data curation, Y.M.; methodology and software, X.F.; validation, X.L. and X.Z.; resources, writing—review and editing and supervision, J.W.

**Funding:** This research was funded by Sichuan Science and Technology Program, grant number 2018JY0451, Education Department of Sichuan Province, grant number 17CZ0019 and 17ZA0218, Youth Innovation Promotion Association CAS, grant number 2019423 and National Innovation and Entrepreneurship Training Program for Undergraduate, grant number X2019018.

**Conflicts of Interest:** The authors declare no conflict of interest.

## References

1. Peiris, C.; Gunatilake, S.R.; Mlsna, T.E.; Mohan, D.; Vithanage, M. Biochar based removal of antibiotic sulfonamides and tetracyclines in aquatic environments: A critical review. *Bioresour. Technol.* **2017**, *246*, 150–159. [[CrossRef](#)] [[PubMed](#)]
2. Zhang, Y.; Shi, J.; Xu, Z.; Chen, Y.; Song, D. Degradation of tetracycline in a schorl/H<sub>2</sub>O<sub>2</sub> system: Proposed mechanism and intermediates. *Chemosphere* **2018**, *202*, 661–668. [[CrossRef](#)] [[PubMed](#)]
3. Mirsoleimani-Azizi, S.M.; Setoodeh, P.; Zeinali, S.; Rahimpour, M.R. Tetracycline antibiotic removal from aqueous solutions by MOF-5: Adsorption isotherm, kinetic and thermodynamic studies. *J. Environ. Chem. Eng.* **2018**, *6*, 6118–6130. [[CrossRef](#)]
4. Okoli, C.P.; Ofomaja, A.E. Development of sustainable magnetic polyurethane polymer nanocomposite for abatement of tetracycline antibiotics aqueous pollution: Response surface methodology and adsorption dynamics. *J. Clean. Prod.* **2019**, *217*, 42–55. [[CrossRef](#)]
5. Luo, Y.; Chen, J.; Wu, C.; Zhang, J.; Tang, J.; Shang, J.; Liao, Q. Effect of particle size on adsorption of norfloxacin and tetracycline onto suspended particulate matter in lake. *Environ. Pollut.* **2019**, *244*, 549–559. [[CrossRef](#)]
6. Yeşilova, E.; Osman, B.; Kara, A.; Özer, E.T. Molecularly imprinted particle embedded composite cryogel for selective tetracycline adsorption. *Sep. Purif. Technol.* **2018**, *200*, 155–163. [[CrossRef](#)]
7. Ma, Y.; Xiong, H.; Zhao, Z.; Yu, Y.; Zhou, D.; Dong, S. Model-based evaluation of tetracycline hydrochloride removal and mineralization in an intimately coupled photocatalysis and biodegradation reactor. *Chem. Eng. J.* **2018**, *351*, 967–975. [[CrossRef](#)]
8. Xiong, H.; Zou, D.; Zhou, D.; Dong, S.; Wang, J.; Rittman, B.E. Enhancing degradation and mineralization of tetracycline using intimately coupled photocatalysis and biodegradation (ICPB). *Chem. Eng. J.* **2017**, *316*, 7–14. [[CrossRef](#)]
9. Saitoh, T.; Shibata, K.; Hiraide, M. Rapid removal and photodegradation of tetracycline in water by surfactant-assisted coagulation—Sedimentation method. *J. Environ. Chem. Eng.* **2014**, *2*, 1852–1858. [[CrossRef](#)]
10. Saitoh, T.; Shibata, K.; Fujimori, K.; Ohtani, Y. Rapid removal of tetracycline antibiotics from water by coagulation-flotation of sodium dodecyl sulfate and poly (allylamine hydrochloride) in the presence of Al(III) ions. *Sep. Purif. Technol.* **2017**, *187*, 76–83. [[CrossRef](#)]
11. Zhang, N.; Chen, J.; Fang, Z.; Tsang, E.P. Ceria accelerated nanoscale zerovalent iron assisted heterogenous Fenton oxidation of tetracycline. *Chem. Eng. J.* **2019**, *369*, 588–599. [[CrossRef](#)]

12. Taşkan, B.; Casey, E.; Hasar, H. Simultaneous oxidation of ammonium and tetracycline in a membrane aerated biofilm reactor. *Sci. Total Environ.* **2019**, *682*, 553–560. [[CrossRef](#)] [[PubMed](#)]
13. Zhang, Y.; Zhou, J.; Chen, X.; Wang, L.; Cai, W. Coupling of heterogeneous advanced oxidation processes and photocatalysis in efficient degradation of tetracycline hydrochloride by Fe-based MOFs: Synergistic effect and degradation pathway. *Chem. Eng. J.* **2019**, *369*, 745–757. [[CrossRef](#)]
14. Sun, W.; Sun, Y.; Shah, K.J.; Chiang, P.C.; Zheng, H. Electrocatalytic oxidation of tetracycline by Bi-Sn-Sb/ $\gamma$ -Al<sub>2</sub>O<sub>3</sub> three-dimensional particle electrode. *J. Hazard. Mater.* **2019**, *370*, 24–32. [[CrossRef](#)] [[PubMed](#)]
15. Zheng, X.; Wang, K.; Huang, Z.; Liu, Y.; Wen, J.; Peng, H. MgO nanosheets with N-doped carbon coating for the efficient visible-light photocatalysis. *J. Ind. Eng. Chem.* **2019**, *76*, 288–295. [[CrossRef](#)]
16. Zheng, X.; Fu, W.; Kang, F.; Peng, H.; Wen, J. Enhanced photo-Fenton degradation of tetracycline using TiO<sub>2</sub>-coated  $\alpha$ -Fe<sub>2</sub>O<sub>3</sub> core-shell heterojunction. *J. Ind. Eng. Chem.* **2018**, *68*, 14–23. [[CrossRef](#)]
17. Ma, Y.; Lv, C.; Hou, J.; Yuan, S.; Wang, Y.; Xu, P.; Gao, G.; Shi, J. 3D hollow hierarchical structures based on 1D BiOCl nanorods intersected with 2D Bi<sub>2</sub>WO<sub>6</sub> nanosheets for efficient photocatalysis under visible light. *Nanomaterials* **2019**, *9*, 322. [[CrossRef](#)] [[PubMed](#)]
18. Tian, L.; Rui, Y.; Sun, K.; Cui, W.; An, W. Surface Decoration of ZnWO<sub>4</sub> nanorods with Cu<sub>2</sub>O nanoparticles to build heterostructure with enhanced photocatalysis. *Nanomaterials* **2018**, *8*, 33. [[CrossRef](#)]
19. Ye, G.; Yu, Z.; Li, Y.; Li, L.; Song, L.; Gu, L.; Cao, X. Efficient treatment of brine wastewater through a flow-through technology integrating desalination and photocatalysis. *Water Res.* **2019**, *157*, 134–144. [[CrossRef](#)]
20. Negrin-Montecelo, Y.; Testa-Anta, M.; Marin-Caba, L.; Perez-Lorenzo, M.; Salgueirino, V.; Correa-Duarte, M.A.; Comesana-Hermo, M. Titanate nanowires as one-dimensional hot spot generators for broadband Au-TiO<sub>2</sub> photocatalysis. *Nanomaterials* **2019**, *9*, 990. [[CrossRef](#)]
21. Hao, M.; Deng, X.; Xu, L.; Li, Z. Noble metal Free MoS<sub>2</sub>/ZnIn<sub>2</sub>S<sub>4</sub> nanocomposite for acceptorless photocatalytic semi-dehydrogenation of 1,2,3,4-tetrahydroisoquinoline to produce 3,4-dihydroisoquinoline. *Appl. Catal. B Environ.* **2019**, *252*, 18–23. [[CrossRef](#)]
22. Yan, L.; Li, Z.; Sun, M.; Shen, G.; Li, L. Stable and flexible CuInS<sub>2</sub>/ZnS:Al-TiO<sub>2</sub> film for solar-light-driven photodegradation of soil fumigant. *ACS Appl. Mater. Interf.* **2016**, *8*, 20048–20056. [[CrossRef](#)] [[PubMed](#)]
23. Lu, X.; Deng, F.; Liu, M.; Luo, X.; Wang, A. The regulation on visible-light photocatalytic activity of CuInS<sub>2</sub> by different Cu/In molar ratio. *Mater. Chem. Phys.* **2018**, *212*, 372–377. [[CrossRef](#)]
24. Leach, A.D.P.; Mast, L.G.; Hernández-Pagán, E.A.; Macdonald, J.E. Phase dependent visible to near-infrared photoluminescence of CuInS<sub>2</sub> nanocrystals. *J. Mater. Chem. C* **2015**, *3*, 3258–3265. [[CrossRef](#)]
25. Cheng, Z.; Zhan, X.; Wang, F.; Wang, Q.; Xu, K.; Liu, Q.; Jiang, C.; Wang, Z.; He, J. Construction of CuInS<sub>2</sub>/Ag sensitized ZnO nanowire arrays for efficient hydrogen generation. *RSC Adv.* **2015**, *5*, 81723–81727. [[CrossRef](#)]
26. Jia, L.; Wang, Y.; Nie, Q.; Liu, B.; Liu, E.; Hu, X.; Fan, J. Aqueous-synthesis of CuInS<sub>2</sub> core and CuInS<sub>2</sub>/ZnS core/shell quantum dots and their optical properties. *Mater. Lett.* **2017**, *200*, 27–30. [[CrossRef](#)]
27. Enesca, A.; Yamaguchi, Y.; Terashima, C.; Fujishima, A.; Nakata, K.; Duta, A. Enhanced UV-Vis photocatalytic performance of the CuInS<sub>2</sub>/TiO<sub>2</sub>/SnO<sub>2</sub> hetero-structure for air decontamination. *J. Catal.* **2017**, *350*, 174–181. [[CrossRef](#)]
28. Liu, A.; Yu, C.; Lin, J.; Sun, G.; Xu, G.; Huang, Y.; Liu, Z.; Tang, C. Construction of CuInS<sub>2</sub>@ZIF-8 nanocomposites with enhanced photocatalytic activity and durability. *Mater. Res. Bull.* **2019**, *112*, 147–153. [[CrossRef](#)]
29. Hosseinpour-Mashkani, S.M.; Salavati-Niasari, M.; Mohandes, F. CuInS<sub>2</sub> nanostructures: Synthesis, characterization, formation mechanism and solar cell applications. *J. Ind. Eng. Chem.* **2014**, *20*, 3800–3807. [[CrossRef](#)]
30. Kong, L.; Li, Z.; Huang, S.; Jia, J.; Li, L. Boosting photocatalytic performance and stability of CuInS<sub>2</sub>/ZnS-TiO<sub>2</sub> heterostructures via sol-gel processed integrate amorphous titania gel. *Appl. Catal. B Environ.* **2017**, *204*, 403–410. [[CrossRef](#)]
31. Guo, F.; Shi, W.; Li, M.; Shi, Y.; Wen, H. 2D/2D Z-scheme heterojunction of CuInS<sub>2</sub>/g-C<sub>3</sub>N<sub>4</sub> for enhanced visiblelight-driven photocatalytic activity towards the degradation of tetracycline. *Sep. Purif. Technol.* **2019**, *210*, 608–615. [[CrossRef](#)]

32. Luo, S.; Ke, J.; Yuan, M.; Zhang, Q.; Xie, P.; Deng, L.; Wang, S. CuInS<sub>2</sub> quantum dots embedded in Bi<sub>2</sub>WO<sub>6</sub> nanoflowers for enhanced visible light photocatalytic removal of contaminants. *Appl. Catal. B Environ.* **2018**, *221*, 215–222. [[CrossRef](#)]
33. Xie, C.; Lu, X.; Deng, F.; Luo, X.; Gao, J.; Dionysiou, D.D. Unique surface structure of nano-sized CuInS<sub>2</sub> anchored on rGO thin film and its superior photocatalytic activity in real wastewater treatment. *Chem. Eng. J.* **2018**, *338*, 591–598. [[CrossRef](#)]
34. Li, J.; Kempken, B.; Dzhagan, V.; Zahn, D.R.T.; Grzelak, J.; Mackowski, S.; Parisia, J.; Kolny-Olesiak, J. Alloyed CuInS<sub>2</sub>–ZnS nanorods: Synthesis, structure and optical properties. *CrystEngComm* **2015**, *17*, 5634–5643. [[CrossRef](#)]
35. Wang, B.; Li, X.; Cai, X.; Yu, W.; Zhang, L.; Zhao, R.; Ke, S. Blue phosphorus/Mg(OH)<sub>2</sub> van der Waals heterostructures as promising visible-light photocatalysts for water splitting. *J. Phys. Chem. C* **2018**, *122*, 7075–7080. [[CrossRef](#)]
36. Luévano-Hipólito, E.; Torres Martínez, L.M. Mg(OH)<sub>2</sub> films prepared by ink-jet printing and their photocatalytic activity in CO<sub>2</sub> reduction and H<sub>2</sub>O conversion. *Top. Catal.* **2018**, *61*, 1574–1584. [[CrossRef](#)]
37. Pilarska, A.A.; Klapiszewski, L.; Jesionowski, T. Recent development in the synthesis, modification and application of Mg(OH)<sub>2</sub> and MgO: A review. *Powder Technol.* **2017**, *319*, 373–407. [[CrossRef](#)]
38. Ren, K.; Yu, J.; Tang, W. A two-dimensional vertical van der Waals heterostructure based on g-GaN and Mg(OH)<sub>2</sub> used as a promising photocatalyst for water splitting: A first-principles calculation. *J. Appl. Phys.* **2019**, *126*, 065701. [[CrossRef](#)]
39. Flores-Flores, M.; Luévano-Hipólito, E.; Torres-Martínez, L.M.; Do, T.O. CO<sub>2</sub> adsorption and photocatalytic reduction over Mg(OH)<sub>2</sub>/CuO/Cu<sub>2</sub>O under UV-Visible light to solar fuels. *Mater. Chem. Phys.* **2019**, *227*, 90–97. [[CrossRef](#)]
40. Yagmurcukardes, M.; Torun, E.; Senger, R.T.; Peeters, F.M.; Sahin, H. Mg(OH)<sub>2</sub>-WS<sub>2</sub> van der Waals heterobilayer: Electric field tunable band-gap crossover. *Phys. Rev. B* **2016**, *94*, 195403. [[CrossRef](#)]
41. Wang, F.; Cui, A.; Sun, H.; Zhou, B.; Xu, L.; Jiang, K.; Shang, L.; Hu, Z.; Chu, J. Electronic bandgap manipulation of monolayer WS<sub>2</sub> by vertically coupled insulated Mg(OH)<sub>2</sub> layers. *J. Alloy. Compd.* **2019**, *785*, 156–162. [[CrossRef](#)]
42. Suslu, A.; Wu, K.; Sahin, H.; Chen, B.; Yang, S.; Cai, H.; Aoki, T.; Horzum, S.; Kang, J.; Peeters, F.M. Unusual dimensionality effects and surface charge density in 2D Mg(OH)<sub>2</sub>. *Sci. Rep.* **2016**, *6*, 20525. [[CrossRef](#)] [[PubMed](#)]
43. Bacaksiz, C.; Dominguez, A.; Rubio, A.; Senger, R.T.; Sahin, H. h-AlN-Mg(OH)<sub>2</sub> van der Waals bilayer heterostructure: Tuning the excitonic characteristics. *Phys. Rev. B* **2017**, *95*, 075423. [[CrossRef](#)]
44. Zheng, X.; Huang, M.; You, Y.; Fu, X.; Liu, Y.; Wen, J. One-pot synthesis of sandwich-like MgO@Carbon with enhanced sorption capacity of organic dye. *Chem. Eng. J.* **2018**, *334*, 1399–1409. [[CrossRef](#)]
45. Ren, K.; Yu, J.; Tang, W. First-principles study of two-dimensional van der Waals heterostructure based on ZnO and Mg(OH)<sub>2</sub>: A potential photocatalyst for water splitting. *Phys. Lett. A* **2019**, *383*, 125916. [[CrossRef](#)]
46. Luo, Y.; Wang, S.; Ren, K.; Chou, J.; Yu, J.; Sun, Z.; Sun, M. Transition-metal dichalcogenides/Mg(OH)<sub>2</sub> van der Waals heterostructures as promising water-splitting photocatalysts: A first-principles study. *Phys. Chem. Chem. Phys.* **2019**, *21*, 1791. [[CrossRef](#)]
47. Xia, C.; Xiong, W.; Du, J.; Wang, T.; Wei, Z.; Li, J. Robust electronic and mechanical properties to layer number in 2D wide-gap X(OH)<sub>2</sub> (X=Mg, Ca). *J. Phys. Appl. Phys.* **2018**, *51*, 015107. [[CrossRef](#)]
48. Wu, B.; Lu, S.; Xu, W.; Cui, S.; Li, J.; Han, P. Study on corrosion resistance and photocatalysis of cobalt superhydrophobic coating on aluminum substrate. *Surf. Coat. Technol.* **2017**, *350*, 174–181. [[CrossRef](#)]
49. Liu, X.; Lv, S.; Fan, B.; Xing, A.; Jia, B. Ferroelectric polarization-enhanced photocatalysis in BaTiO<sub>3</sub>-TiO<sub>2</sub> core-shell heterostructures. *Nanomaterials* **2019**, *9*, 1116. [[CrossRef](#)]
50. Liu, Y.; Wang, K.; Huang, Z.; Zheng, X.; Wen, J. Enhanced photo-Fenton activity of Sm<sub>2</sub>O<sub>3</sub>-NiO heterojunction under visible light irradiation. *J. Alloy. Compd.* **2019**, *800*, 498–504. [[CrossRef](#)]
51. Zheng, X.; Li, X.; Peng, H.; Wen, J. Ag-decorated core-shell Sm<sub>2</sub>O<sub>3</sub>@TiO<sub>2</sub> nanocomposites with enhanced visible-light photocatalytic performance. *J. Phys. Chem. Solids* **2018**, *123*, 206–215. [[CrossRef](#)]
52. Zeng, J.; Li, Z.; Peng, H.; Zheng, X. Core-shell Sm<sub>2</sub>O<sub>3</sub>@ZnO nano-heterostructure for the visible light driven photocatalytic performance. *Coll. Surf. A* **2019**, *560*, 244–251. [[CrossRef](#)]
53. Zheng, X.; Huang, M.; You, Y.; Peng, H.; Wen, J. Core-shell structured α-Fe<sub>2</sub>O<sub>3</sub>@CeO<sub>2</sub> heterojunction for the enhanced visible-light photocatalytic activity. *Mater. Res. Bull.* **2018**, *101*, 20–28. [[CrossRef](#)]

54. Rayaroth, M.P.; Aravind, U.K.; Aravindakumar, C.T. Effect of inorganic ions on the ultrasound initiated degradation and product formation of triphenylmethane dyes. *Ultrason. Sonochem.* **2018**, *48*, 482–491. [[CrossRef](#)] [[PubMed](#)]
55. Wang, X.; Jia, J.; Wang, Y. Combination of photocatalysis with hydrodynamic cavitation for degradation of tetracycline. *Chem. Eng. J.* **2017**, *315*, 274–282. [[CrossRef](#)]
56. Lin, Z.Y.; Liu, P.; Yan, J.H.; Yang, G.W. Matching energy levels between TiO<sub>2</sub> and α-Fe<sub>2</sub>O<sub>3</sub> in a core-shell nanoparticle for the visible-light photocatalysis. *J. Mater. Chem. A* **2015**, *3*, 14853–14863. [[CrossRef](#)]
57. Abdel-Wahab, A.M.; Al-Shirbini, A.S.; Mohamed, O.; Nasr, O. Photocatalytic degradation of paracetamol over magnetic flower-like TiO<sub>2</sub>/Fe<sub>2</sub>O<sub>3</sub> core-shell nanostructures. *J. Photochem. Photobiol. A* **2017**, *347*, 186–198. [[CrossRef](#)]
58. Liu, J.; Yang, S.; Wu, W.; Tian, Q.; Cui, S.; Dai, Z.; Ren, F.; Xiao, X.; Jiang, C. 3D flowerlike α-Fe<sub>2</sub>O<sub>3</sub>@TiO<sub>2</sub> core-shell nanostructures: General synthesis and enhanced photocatalytic performance. *ACS Sustain. Chem. Eng.* **2015**, *3*, 2975–2984. [[CrossRef](#)]
59. Chen, M.; Shen, X.; Wu, Q.H.; Li, W.; Diao, G.W. Template-assisted synthesis of core-shell α-Fe<sub>2</sub>O<sub>3</sub>@TiO<sub>2</sub> nanorods and their photocatalytic property. *J. Mater. Sci.* **2015**, *50*, 4083–4094. [[CrossRef](#)]
60. Reyes, C.; Fernández, J.; Freer, J.; Mondaca, M.A.; Zaror, C.; Malato, S.; Mansilla, H.D. Degradation and inactivation of tetracycline by TiO<sub>2</sub> photocatalysis. *J. Photochem. Photobiol. A* **2006**, *184*, 141–146. [[CrossRef](#)]



© 2019 by the authors. Licensee MDPI, Basel, Switzerland. This article is an open access article distributed under the terms and conditions of the Creative Commons Attribution (CC BY) license (<http://creativecommons.org/licenses/by/4.0/>).